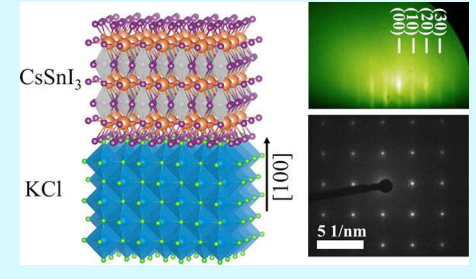


# **Epitaxial Stabilization of Tetragonal Cesium Tin Iodide**

Lili Wang, Pei Chen, Padmanaban S. Kuttipillai, Isaac King, Richard Staples, Kai Sun, and Richard R. Lunt\*,†,§

Supporting Information

ABSTRACT: A full range of optoelectronic devices has been demonstrated incorporating hybrid organic-inorganic halide perovskites including highperformance photovoltaics, light emitting diodes, and lasers. Tin-based inorganic CsSnIhalide perovskites, such as CsSnX<sub>3</sub> (X = Cl, Br, I), have been studied as promising candidates that avoid toxic lead halide compositions. One of the main obstacles for improving the properties of all-inorganic perovskites and transitioning their use to high-end electronic applications is obtaining crystalline thin films with minimal crystal defects, despite their reputation for defect tolerance in photovoltaic applications. In this study, the single-domain epitaxial growth of cesium tin iodide (CsSnI<sub>3</sub>) on closely lattice matched single-crystal



potassium chloride (KCl) substrates is demonstrated. Using in situ real-time diffraction techniques, we find a new epitaxiallystabilized tetragonal phase at room temperature that expands the possibility for controlling electronic properties. We also exploit controllable epitaxy to grow multilayer two-dimensional quantum wells and demonstrate epitaxial films in a lateral photodetector architecture. This work provides insight into the phase control during halide perovskite epitaxy and expands the selection of epitaxially accessible materials from this exciting class of compounds.

KEYWORDS: halide perovskite, epitaxy, vapor-deposition, 2D quantum well, photodetector

## ■ INTRODUCTION

Halide perovskites have shown great potential for a wide range of applications in solar harvesting, 1-4 light emission, 5-8 lasing, 9-12 quantum dots, 13-17 water splitting, 18-20 and thinfilm electronics.<sup>21–29</sup> Despite the incredibly fast development of their applications in energy conversion, 30 particularly with lead-based compositions, the main hindrances of structural defects, 31,32 trap states, 33 toxicity of lead, 34,35 and the instability of organic components 55-39 remain a challenge.  $CsSnX_3$  perovskites (X = Cl, Br, I) have been investigated as inorganic and lead-free alternatives. 40-44 However, compared with lead halide perovskites, the crystalline thin-film fabrication of CsSnX3 has been more challenging and has limited development in high-performance photovoltaics and optoelectronics due to a lower defect tolerance.

Another critical challenge for improving the optoelectronic performance of CsSnX3-based devices is controlling the phase during film growth. For cesium tin iodide (CsSnI<sub>3</sub>), four different phases can form depending on the temperature including cubic (B- $\alpha$ ), tetragonal (B- $\beta$ ), orthorhombic (black, B-γ), and orthorhombic (yellow, Y) phases where only the orthorhombic (black) and orthorhombic (yellow) phases are stable at room temperature. 45,46 These phases have different optical and electronic properties, which impact carrier transport. To date, most research on CsSnI<sub>3</sub> focuses on the orthorhombic (black, B- $\gamma$ ) phase as the absorber layer.<sup>47</sup> However, there has been little work on the cubic and tetragonal phases since they are both unstable at room temperature.

Epitaxial growth has long been utilized to achieve the lowest defect densities and highest performance for applications in lasers, thin-film transistors, two-dimensional (2D) electron gases, sensors, and high-power devices. The development of inorganic materials such as III-V semiconductors has been extensively accelerated by epitaxial growth. Moreover, studies of epitaxial oxide perovskites have shown that unique properties can occur at the interfaces of different materials including superconductivity, ferroelectricity, and magnetism. These functional properties can be tuned by engineering the symmetries and degrees of freedom of correlated electrons at the interfaces of oxide perovskites, which is associated with the atomic arrangement at the interface. 48-51 Thus, epitaxial growth provides precise interface control and correspondingly yields the potential for interesting new systems such as magnetic superconductors, noncentrosymmetric superconductors, and multiferroics. 52-56 These successes have driven a new focus to control film quality, defect density, strain, and phases of new semiconducting materials that should be applicable to halide perovskites. Recently, the demonstration of controllable epitaxial growth of CsSnBr<sub>3</sub> on metal halide salts,<sup>57</sup> thick

Received: April 5, 2019 Accepted: June 24, 2019 Published: June 24, 2019

<sup>&</sup>lt;sup>†</sup>Department of Chemical Engineering and Materials Science, <sup>‡</sup>Department of Chemistry, and <sup>§</sup>Department of Physics and Astronomy, Michigan State University, East Lansing, Michigan 48824, United States

 $<sup>^{\</sup>parallel}$ Department of Materials Science and Engineering, University of Michigan, Ann Arbor, Michigan 48109, United States

**ACS Applied Materials & Interfaces** 

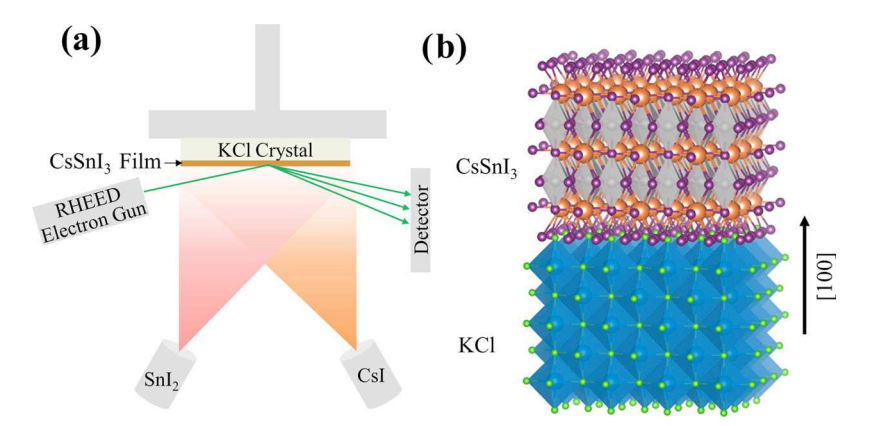


Figure 1. (A) Thin-film CsSnI<sub>3</sub> is grown epitaxially on a single crystalline KCl(100) substrate with two precursors, CsI and SnI<sub>3</sub> (1:1) monitored by RHEED in situ and real time. (B) A schematic of the epitaxial structure of the CsSnI3 film on KCl(100) (Cs: orange; Sn: gray; I: purple; K: blue; Cl: light green).

quasiepitaxial growth of CsPbBr<sub>3</sub>,<sup>58</sup> and epitaxial nanoplatelets of CsPbBr<sub>3</sub> on strontium titanate<sup>59,60</sup> has confirmed the feasibility of vapor-phase epitaxial growth methods for this group of materials.

In this study, the room-temperature epitaxial growth of CsSnI<sub>3</sub> on single crystalline alkali halide salt substrate KCl is demonstrated. The substrate was chosen to closely match the high-temperature cubic phase lattice constants and maintain similar ionic bonding character of the film. However, we find that the epitaxial growths lead to a new stable tetragonal phase at room temperature that has a and b lattice constants similar to the high-temperature cubic phase. This "epitaxial stabilization" method provides an approach to stabilize a metastable phase. The impact of strain is explored by tuning substrate lattice constants via alloyed interlayer deposition. Exploiting the precise growth enabled by vapor-phase epitaxy, we also explore the quantum confinement effect in this material and determine a surprisingly small effective Bohr radius. Finally, epitaxial films of CsSnI3 are integrated into a lateral photodetector application with good photoresponse. This work provides new insight into the stabilization of halide perovskite crystal phases and expands the selection of epitaxial halide perovskites.

#### RESULTS AND DISCUSSION

Epitaxial Growth and Structure Analysis. The epitaxial growth of CsSnI<sub>3</sub> films on single crystalline KCl(100) substrates is achieved using reactive thermal deposition of CsI and SnI<sub>2</sub> with a molar ratio of 1:1, which was monitored in situ and real-time using reflection high-energy electron diffraction (RHEED) with ultralow currents (nanoampere range) to prevent charging and beam damage (Figure 1a). A schematic of the epitaxial growth is shown in Figure 1b. The freshly cleaved KCl substrate exhibits sharp streaky peaks along the [100] direction along with Kikuchi lines indicative of the single crystalline (single domain) and thick nature of the KCl substrates. After growing one monolayer (ML) of CsSnI<sub>3</sub>, the pattern changes, and the KCl Kikuchi patterns disappear. A new set of streaky lines emerges overlapping with the (20) streaks of KCl, along with (10) streaks between the (20) streaks (Figure 2a). These additional streaks are expected as there is a structural change from the face-centered cubic substrate to the primitive cell of the halide perovskite film. These patterns are observed without any substrate rotation, indicating good lattice matching and alignment between the

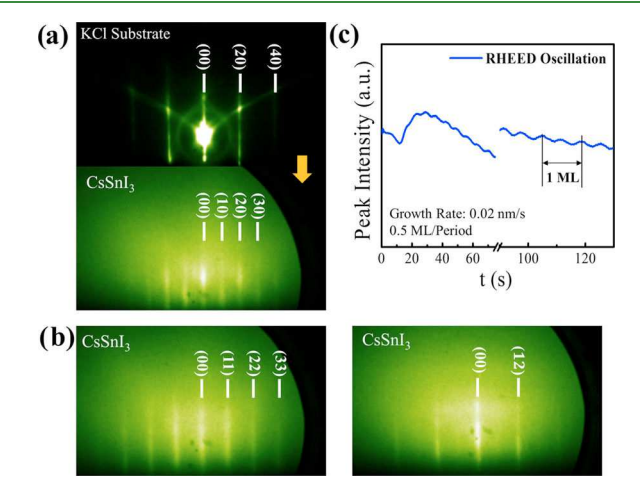


Figure 2. (A) RHEED pattern of the bare KCl substrate and 20 nm of CsSnI<sub>3</sub>. (B) Rotation-dependent RHEED patterns of the smooth CsSnI<sub>3</sub> epitaxial film. (C) RHEED oscillations monitored by capturing the peak intensity change of the central streak of the pattern as a function of time. The observation of 0.5 ML/period is consistent with the epitaxial growth of CsSnI<sub>3</sub> (note that the growth rate 0.02 nm/s is for the reacted film not the sources).

film and the substrate. The streaky RHEED patterns remain essentially unchanged up to and beyond thicknesses of ~20 nm. The streakiness of the pattern is an indication of a smooth crystalline layer, which is consistent with the morphology shown in the scanning electron microscope (SEM) (Figure S1a). To further understand the crystal structure of the CsSnI<sub>3</sub> epitaxial film, RHEED patterns were collected at various azimuthal angles (Figure 2b). The patterns vary as expected for a single crystal, indicating that single-domain growth is achieved across the KCl substrate. From the d-spacing obtained at various azimuthal angles, we obtained the lattice constant of the epitaxial film:  $a = b = 0.622 \pm 0.007$  nm.

During the epitaxial growth, low source deposition rates (<0.02 nm/s) are found to aid in the formation of smoother films and streakier patterns. If the sources are deposited with a much higher growth rate, spotty patterns quickly replace the streaky patterns from the KCl substrate, indicating that a rough crystalline film is formed (Figure S2b). The growth mode was also studied by monitoring the intensity of the RHEED patterns (Figure 2c). When using low source deposition rates, RHEED oscillations are observed indicating Frank-van der Merwe (layer-by-layer) growth mode. Two full cycles of the oscillation are found to correspond to the growth of one ML (half of a complete unit cell) of the CsSnI<sub>3</sub> film as confirmed from ex situ thickness measurements (Figure 2c). This is similar to the observation for epitaxial CsSnBr<sub>3</sub> growth on NaCl.<sup>57</sup>

Under certain growth conditions (e.g., high-rate growth), half-order RHEED streaks sometimes appear, as seen in Figure S3. This indicates the formation of surface reconstruction. In these cases, the half-order streaks fade as the film growth proceeded to higher thickness. Because these streaks are only observed under high growth rates, it is unlikely to be indicative of the underlying growth front mechanism. That is, the growth front does not typically proceed via a surface reconstruction.

Out-of-plane X-ray diffraction (XRD) data was collected to confirm the crystal structure of the epitaxial film (Figure 3a).

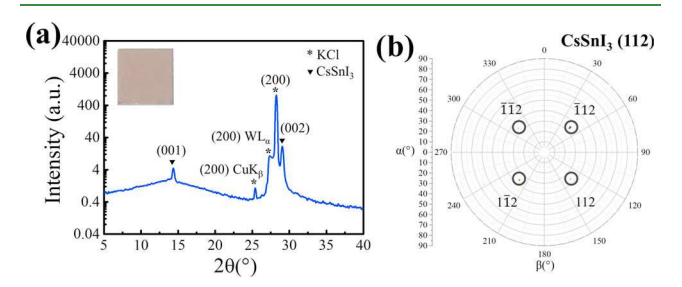


Figure 3. (A) Out-of-plane XRD scan of 40 nm of CsSnI<sub>3</sub> on the KCl substrate and photograph of the film on a 1 cm  $\times$  1 cm substrate. The KCl(200) peak is at 28.35° (Cu K $_{\beta}$  and W L $_{\alpha}$  peaks are seen at 25.50 and 27.42°), and the CsSnI<sub>3</sub>(001) and (002) peaks are at 14.46 and 29.16°. (B) The (112) pole figure scan of 40 nm of CsSnI<sub>3</sub> on KCl.  $\alpha$  and  $\beta$  are the tilt angle and rotation angle, respectively, around the sample surface normal direction. Note that the (112) is not observable for KCl. Additional pole figures of both the film and substrate are provided in the Supporting Information.

The peaks observed at 14.46 and 29.16° are the (001) and (002) of the epitaxial phase, respectively, which gives a lattice constant  $c = 0.612 \pm 0.002$  nm. Combined with the RHEED data, we determine that this is an epitaxial tetragonal (referred to as "epi-tetragonal") phase ( $a = b = 0.622 \pm 0.007$  nm,  $c = 0.612 \pm 0.002$  nm) stabilized by lattice matching with the KCl substrate (a = 0.629 nm) that has a significantly different structure and atomic arrangement from the bulk high-temperature tetragonal phase. The d spacings are well matched with the substrate in the early growth stage (within error) and remain nearly unchanged as the growth proceeds to higher thickness indicating that the growth is pseudomorphic. The (112), (021), and (211) pole figure scans of the film are

shown in Figures 3b and S4b-d. These were chosen as they are clearly distinguishable from any substrate peaks and are not allowed for KCl. The fixed diffraction angles for each pole figure scan are calculated from the lattice constant of the epitetragonal phase. The (112) and (021) pole figures show the expected fourfold symmetry, whereas the (211) scan shows the expected eightfold symmetry (see Figure S4e,f for the simulated pole figures for both KCl and epi-tetragonal  $CsSnI_3$ ). The a/c ratio obtained from the transmission electron microscopy (TEM) high-resolution images of the epitaxial interface is 1.03, which clearly emphasizes the tetragonal nature of the structure and is close to 1.02 obtained from diffraction data (Figure 4). The TEM also clearly confirms the pseudomorphic nature of the film. To further verify the crystal structure, the film was removed from the substrate and folded to obtain a pseudopowder (textured powder) for synchrotron X-ray characterization. This data confirms that the epitaxial film is a new tetragonal phase, as shown in Figure S5. An obvious peak split is seen at 11.28 and 11.39° that corresponds to the (200) and (002) planes of the tetragonal phase. From the synchrotron X-ray data fitting (Figure S6), we obtain lattice constants of the epitaxial film of a = b = 0.6240 nm and c = 0.6178 nm, which are close to and consistent with the XRD and RHEED analysis. The slight difference from the substrate lattice is due to the temperature difference of the scan conditions. Extrapolating the lattice constant from room temperature to 100 K for comparison to the synchrotron data, the lattice constant of the cubic KCl substrate would be  $0.625 \pm 0.001$  nm at 100 K, assuming a thermal expansion coefficient of  $3.2 \times 10^{-5}/\text{K}$ , which is within the error of the in-plane lattice constant measured with the synchrotron data (a = b = 0.6240 nm). This further confirms the pseudomorphic nature of the film and agrees with the findings from TEM.

When determining the crystal structure and phases of these compounds, it is important to consider the oxidation states. For example,  $\mathrm{Sn^{2+}}$  and  $\mathrm{Sn^{4+}}$  oxidation states have been observed in this class of materials, which leads to other analogues such as  $\mathrm{Cs_2SnI_6}$  (cubic,  $a=1.165~\mathrm{nm^{62}}$ ). This phase is ruled out from the simulated diffraction patterns (Figure S7). Furthermore, we confirm the chemical state of Sn and the ratio of these three elements with X-ray photoelectron spectroscopy (XPS). The ratio matches the stoichiometry of  $\mathrm{CsSnI_3}$ , and the Sn is found to have a +2 valence state in the epitaxial film (Figure S8). We note that we do observe a phase transformation from  $\mathrm{CsSnI_3}$  to  $\mathrm{Cs_2SnI_6}$  when epitaxial films are exposed to air for more than 20 h (Figure S9a,b). This is consistent with other reports for the B- $\gamma$  and Y phases of  $\mathrm{CsSnI_3}$ . However, we do not observe this transformation for

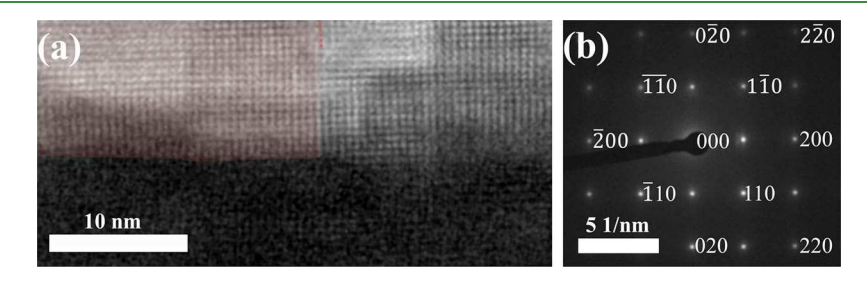


Figure 4. (A) Cross-sectional high-resolution TEM (HRTEM) image at the interface. The film is shaded in red on the left side of the image. Note a substrate step can be observed just to the bottom right of the shading. (B) Selected area electron diffraction (SAED) pattern of the film clearly indicating the tetragonal nature of the crystal structure.

films kept in a N2 environment under dark conditions or under illumination ( $\sim$ 1 sun) (Figure S9c-e).

Both the high-temperature tetragonal and cubic phases are unstable at room temperature.<sup>64</sup> Epitaxy has been commonly deployed to grow metastable phases at a lower temperature. The mechanism for stabilization can include pseudomorphism (strain accommodating lattice matching) or superstructures, whereas relaxation past a critical thickness would result in a bulk structure. In our case, pseudomorphism is the dominant mechanism (seen directly in the high-resolution TEM and synchrotron data) where lattice matching constraints result in a phase that looks similar to the high-temperature cubic phase but exhibits tetragonal distortion to accommodate the tensile strain and perovskite octahedra.

We subsequently utilized the growth on other halide crystal salts with much larger lattice misfit (>10%) to emphasize the control over the resulting phase. When changing the substrate to KBr (a = 0.660 nm), 45 growth of the orthorhombic phase was observed from RHEED and XRD (Figure \$10). The RHEED pattern of the film grown on KBr substrate shows the formation of rotated microdomains. The increase in misfit strain to a value where the critical thickness is less than a monolayer results in unstrained incommensurate (quasiepitaxial) film growth that then exhibits the expected roomtemperature orthorhombic phase.

As we have shown previously, misfit strain between the substrate and the film can be reduced using lattice engineering by alloying epitaxial metal halide interlayer films. 57 For CsSnI<sub>3</sub> growth, a thin alloyed layer (6 nm) of KCl and NaCl with a ratio of 6.7:1 is grown homoepitaxially on the KCl substrate to provide a near-ideal lattice match to the halide perovskite. Streaky RHEED patterns of the alloyed layer and the epitaxial CsSnI<sub>3</sub> layer are shown in Figure S11. By adding a tuned pseudomorphic interlayer of alloyed alkali halide salts, the misfit defect concentration is likely to be reduced even further.

Optical Properties and Quantum Well Fabrication. The optical properties of the CsSnI3 epi-tetragonal phase on KCl were studied (Figure 5). The band gap energies were

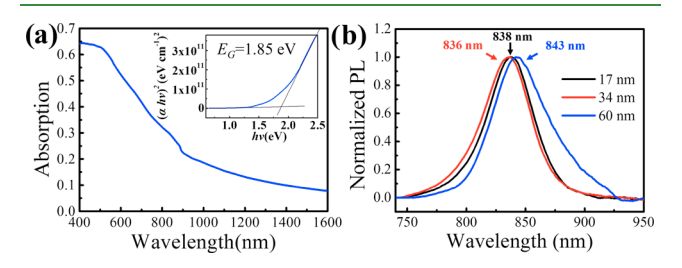


Figure 5. (A) Absorption spectrum of 40 nm CsSnI<sub>3</sub> grown on the KCl substrate. The absolute absorption from the film is plotted. The Tauc plot shows the extrapolation of a direct bandgap of 1.85 eV (inset). (B) PL spectra of quantum wells with well widths of 17, 34, and 60 nm showing peaks at 838, 836, and 843 nm, respectively.

extracted with a Tauc plot, giving a direct band gap of 1.85 eV (Figure 5a, inset). This value is consistent with the photoluminescence (PL) peak emission and onset emission at 1.47 and 1.60 eV. The simulated bandgap of all of the relevant phases is shown in Table S1 using the B3LYP hybrid functional. The epi-tetragonal bandgap is calculated to be 2.07 eV. This overestimation from the simulation is consistent with slight overestimation for the orthorhombic phase (1.40 eV from simulation and 1.31 eV from experiment<sup>66</sup>). This

bandgap is notably distinct from the high-temperature tetragonal phase of 0.41 eV. As discussed above, the epitaxial growth allows the stabilization of a new epi-tetragonal CsSnI<sub>3</sub> phase. Thus, the observation of a larger bandgap is not surprising.

Quantum wells were fabricated with the halide perovskite as the well, and KCl was used as a barrier to study the quantum confinement effect. KCl was grown using a similar method to the homoepitaxy of NaCl reported previously.<sup>67</sup> RHEED was used during growth to confirm that each layer was crystalline and smooth as indicated by streaky patterns. PL spectra of the quantum wells show that by varying well width from 60 to 34 nm, the PL peak shifts modestly from 843 to 836 nm. This indicates that the Bohr radius of CsSnI<sub>3</sub> is relatively small (<10 nm). A similarly small quantum confinement effect has been reported for CsSnBr<sub>3</sub> nanocrystals and CsSnBr<sub>3</sub> quantum wells. 40,57

Photodetector Fabrication with Epitaxial CsSnl<sub>3</sub> Thin Film. Single crystalline CsSnI<sub>3</sub> thin-film-based photodetectors were fabricated with the architecture shown in Figure 6a (see

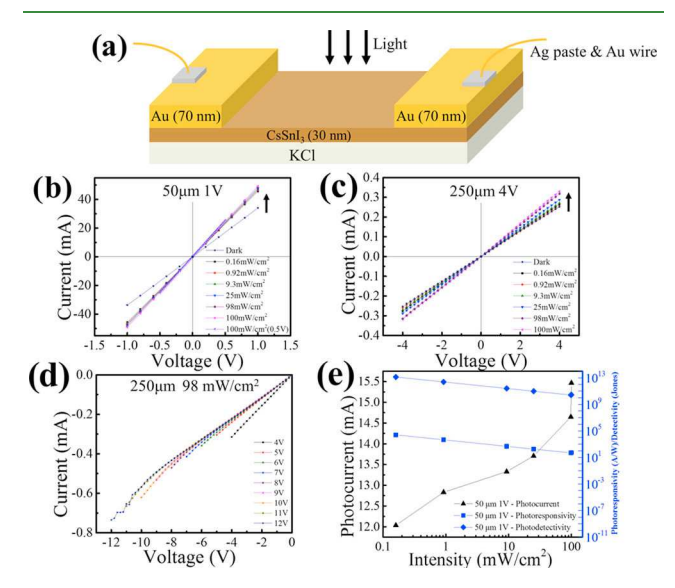


Figure 6. (A) Architecture of single crystalline CsSnI<sub>3</sub> thin-film-based photodetector. Devices with 50 and 250  $\mu$ m channel width are fabricated and tested using simulated AM1.5 G solar illumination. (B) I-V characteristics of the device with 50  $\mu$ m-wide channel width under different illuminations. The arrows indicate the increase in the current when increasing the light intensity. (C) I-V characteristics of the device with 250  $\mu$ m-wide channel width under different illuminations. (D) I-V characteristics of the device with 250  $\mu$ mwide channel width under different testing voltages. (E) Photocurrent (black triangles), photoresponsivity (blue squares), and specific detectivity (blue diamonds) of the device with 50  $\mu$ m-wide channel at 1 V.

the Materials and Methods section for fabrication details). The CsSnI<sub>3</sub> film serves as the photosensitive material to absorb light, and Au electrodes were vapor-deposited on the epitaxial CsSnI<sub>3</sub> layer to collect photogenerated charge carriers. The symmetrical and linear characteristics of the current-voltage (I-V) curve indicate the ohmic contact between the Au electrode and CsSnI<sub>3</sub>. When the channel width between the two Au electrodes is 50  $\mu$ m, the photocurrent is over 2 magnitudes higher than the photocurrent obtained with 250 µm-wide channel. This indicates that the width of the depletion region is less than 250  $\mu$ m. In Figure 6e, the photocurrent is shown to continuously increase with increasing illumination intensity. It is noted that the photocurrent increases significantly faster at the lower range of illumination intensity. The responsivity (R) is a key parameter commonly utilized to evaluate the performance of a photodetector. The responsivity is calculated as

$$R = \frac{I_{\text{light}} - I_{\text{dark}}}{P_{\text{incident}} \times A} \tag{1}$$

where  $I_{\text{light}}$  and  $I_{\text{dark}}$  represent the current measured with or without light illumination, respectively,  $P_{\text{incident}}$  is the incident light power density, and A is the active area. R is typically reported as a function of wavelength but can also be reported for broadband light sources. For this proof-of-principle demonstration, we utilize the average incident white-light power since we were better able to characterize the incident power density of white light versus monochromatic light in this configuration. As shown in Figure 6e, the responsivity exhibits different trends from the photocurrent. As the responsivity is closely correlated to quantum efficiency, the quantum efficiency then decreases with increasing intensity. This reduction is likely due to an accumulation of space charge that creates additional carrier scattering and has been shown to turn off halide perovskite solar cells.<sup>68</sup> Nonetheless, the photocurrent is significantly higher than in the solutionprocessed lead-based hybrid halide perovskite CH3NH3PbI3 incorporated in similar device configurations. 69 For the photodetector under an applied bias, the specific detectivity (D\*) is limited by Shot noise as

$$D^* = \frac{R}{\sqrt{2qJ_{\text{dark}}}} \tag{2}$$

where q is the electron charge and  $J_{\rm dark}$  is the dark current density. The average white-light detectivity gives a value of  $1.32 \times 10^{13}$  Jones (cm Hz<sup>1/2</sup>/W).

## CONCLUSIONS

In summary, the room-temperature epitaxial growth of CsSnI<sub>3</sub> on low-cost metal halide crystals is achieved via reactive thermal deposition and characterized by in situ and ex situ diffraction techniques. This growth is investigated on KCl(100), KBr(100), and alloyed (NaCl/KCl) interlayers on KCl. The growth on KCl(100) reveals a new roomtemperature epitaxial tetragonal phase of CsSnI3 that is closely lattice matched (psuedomorphic) to the KCl. In contrast, the growth observed on KBr (with large misfit) results in quasiepitaxial films with the orthorhombic phase (common room-temperature phase) and rotated microdomains. The epitaxial growth of CsSnI3 is furher exploited to demonstrate multilayer epitaxial quantum wells and lateral photodetectors. This work provides insight into the control over phase and ordering during halide perovskite epitaxial growth and expands the selection of photoactive materials for growing epitaxial halide perovskites that can be exploited in high-performance electronic applications.

#### MATERIALS AND METHODS

**Epitaxial Film and Quantum Well Growth.** The epitaxial growth of  $CsSnI_3$  was carried out by co-evaporating the precursors CsI and  $SnI_2$  in a customized multisource thermal evaporator (Angstrom Engineering). Prior to growth, KCl single-crystal substrates were cleaved to expose the fresh (100) surfaces in a

glovebox. The growth method as well as the in situ and real-time characterization techniques have been discussed in detail in our previous report. The capability of performing low-current RHEED on insulating halide crystals has also been demonstrated in our previous studies. Similar growth conditions are used for the fabrication of quantum well multilayers. Epitaxial KCl (barrier layer) was vapor-deposited from a KCl powder source with a rate of 0.002 nm/s and a barrier thickness of 1.5 nm.

**Material Characterization.** Details on cross-sectional TEM, SEM, XPS, PL, and UV–Vis measurments have been discussed in detail in our previous report.<sup>57</sup> Note that nitrogen gas was purged during both PL and UV–Vis measurements to protect the sample during the scan.

Out-of-plane XRD and pole figures were obtained using an XRD instrument with a Cu  $K_{\alpha}$  source at 40 kV and 44 mA and using a Ni filter (Rigaku SmartLab). The sample was placed in a nitrogen-sealed dome to protect it from oxygen and moisture during the scan but also reduces the intensity of the film peaks. Synchrotron XRD data were collected at the NE-CAT beamline 24-ID-C, Advanced Photon Source (wavelength: 0.0619870 nm). The sample was prepared by carefully cleaving the single crystalline epitaxial film from the substrate and mounting/folding the film onto a copper holder stored at liquid nitrogen during transferring. The data were processed with XDS as implemented in rapid automated processing of X-ray data (https://github.com/RAPD/RAPD).

**Photodetector Fabrication.** Lateral photodetectors were fabricated by depositing Au film (70 nm) onto the epitaxial  $CsSnI_3$  single crystalline film by e-beam deposition. The channel between the two Au electrode was fabricated by placing an Au wire (diameter 50  $\mu$ m, Alfa Aesar) or a Cu wire (diameter 250  $\mu$ m, Alfa Aesar) over the  $CsSnI_3$  film as the mask to form the channel region.

**Photocurrent Measurement.** Silver paste (Ted Pella) was used to fix a gold wire onto each Au electrode for better electrical connection. The gold wires of both electrodes were connected to a customized photocurrent set-up, which has been described in details in our previous report.<sup>57</sup>

**Band gap Simulation.** Band structures and bandgap calculations were performed using the CASTEP module in Material Studio 7.0 with the B3LYP functional (300 eV cutoff energy with the k-points set to  $2 \times 2 \times 2$  for the Brillouin zone integration).

## ASSOCIATED CONTENT

# **S** Supporting Information

The Supporting Information is available free of charge on the ACS Publications website at DOI: 10.1021/acsami.9b05592.

Summary of CsSnI<sub>3</sub> phases (Table S1); scanning electron microscope (SEM) image of epi-tetragonal CsSnI<sub>3</sub> (Figure S1); reflection high-energy electron diffraction (RHEED) patterns of high-rate CsSnI<sub>3</sub> epitaxial growth (Figure S2); RHEED patterns for surface reconstruction (Figure S3); pole figure scans of KCl and epi-tetragonal CsSnI<sub>3</sub> (Figure S4); synchrotron X-ray diffraction (XRD) patterns of epi-tetragonal CsSnI<sub>3</sub> (Figures S5 and S6); simulated diffraction patterns of Cs<sub>2</sub>SnI<sub>6</sub> (Figure S7); X-ray photoelectron spectroscopy (XPS) scans of epi-tetragonal CsSnI<sub>3</sub> (Figure S8), epi-tetragonal CsSnI<sub>3</sub> film stability test (Figure S9), CsSnI<sub>3</sub> growth on KBr (Figure S10), and CsSnI<sub>3</sub> growth on a pseudomorphic buffer layer (Figure S11) (PDF)

### AUTHOR INFORMATION

#### **Corresponding Author**

\*E-mail: rlunt@msu.edu.

ORCID ®

Richard Staples: 0000-0003-2760-769X

Kai Sun: 0000-0003-1745-9136

Richard R. Lunt: 0000-0003-4248-6312

#### **Author Contributions**

L.W. and P.C. contributed equally to this work. R.R.L., L.W., and P.C. conceived the project and wrote the manuscript. L.W. and P.C. performed the epitaxial growth, RHEED, XRD, 2D quantum well fabrication, UV-Vis and PL measurements. P.C. performed the pole figure scans. I.K. helped with the film thickness calibration and growth. L.W. fabricated the photodetector and performed measurements. P.S.K. helped with PL measurements. K.S. performed the TEM. R.S. prepared the synchrotron sample and aided in the analysis.

#### **Notes**

The authors declare no competing financial interest.

#### ACKNOWLEDGMENTS

The work at Michigan State University was supported by the National Science Foundation (NSF SSMC 1807573). The FEI Nova 200 Nanolab SEM/FIB and the JEOL-JEM 3100R05 Double Cs-corrected TEM/STEM were under the support of the University of Michigan College of Engineering and NSF grant #DMR-0320740 and NSF grant #DMR-0723032, respectively. The authors thank Chenchen Yang and Dr. Per Askeland for the help with the UV—Vis measurements and thank Dr. Dianyi Liu for useful discussions.

#### REFERENCES

- (1) Kojima, A.; Teshima, K.; Shirai, Y.; Miyasaka, T. Organometal Halide Perovskites as Visible-Light Sensitizers for Photovoltaic Cells. *J. Am. Chem. Soc.* **2009**, *131*, 6050–6051.
- (2) Lee, M. M.; Teuscher, J.; Miyasaka, T.; Murakami, T. N.; Snaith, H. J. Efficient Hybrid Solar Cells Based on Meso-Superstructured Organometal Halide Perovskites. *Science* **2012**, *338*, 643–647.
- (3) Ball, J. M.; Lee, M. M.; Hey, A.; Snaith, H. J. Low-Temperature Processed Meso-Superstructured to Thin-Film Perovskite Solar Cells. *Energy Environ. Sci.* **2013**, *6*, 1739–1743.
- (4) Kazim, S.; Nazeeruddin, M. K.; Grätzel, M.; Ahmad, S. Perovskite as Light Harvester: A Game Changer in Photovoltaics. *Angew. Chem., Int. Ed.* **2014**, *53*, 2812–2824.
- (5) Gong, X.; Yang, Z.; Walters, G.; Comin, R.; Ning, Z.; Beauregard, E.; Adinolfi, V.; Voznyy, O.; Sargent, E. H. Highly Efficient Quantum Dot Near-Infrared Light-Emitting Diodes. *Nat. Photonics* **2016**, *10*, 253–257.
- (6) Yuan, M.; Quan, L. N.; Comin, R.; Walters, G.; Sabatini, R.; Voznyy, O.; Hoogland, S.; Zhao, Y.; Beauregard, E. M.; Kanjanaboos, P.; et al. Perovskite Energy Funnels for Efficient Light-Emitting Diodes. *Nat. Nanotechnol.* **2016**, 872–877.
- (7) Kim, Y.-H.; Cho, H.; Lee, T.-W. Metal Halide Perovskite Light Emitters. *Proc. Natl. Acad. Sci.* **2016**, 11694–11702.
- (8) Hoye, R. L.; Chua, M. R.; Musselman, K. P.; Li, G.; Lai, M. L.; Tan, Z. K.; Greenham, N. C.; MacManus-Driscoll, J. L.; Friend, R. H.; Credgington, D. Enhanced Performance in Fluorene-Free Organometal Halide Perovskite Light-Emitting Diodes using Tunable, Low Electron Affinity Oxide Electron Injectors. *Adv. Mater.* **2015**, 27, 1414–1419.
- (9) Sutherland, B. R.; Hoogland, S.; Adachi, M. M.; Wong, C. T.; Sargent, E. H. Conformal Organohalide Perovskites Enable Lasing on Spherical Resonators. *ACS Nano* **2014**, *8*, 10947–10952.
- (10) Wang, Y.; Li, X.; Song, J.; Xiao, L.; Zeng, H.; Sun, H. All-Inorganic Colloidal Perovskite Quantum Dots: A New Class of Lasing Materials with Favorable Characteristics. *Adv. Mater.* **2015**, 27, 7101–7108.
- (11) Xing, G.; Kumar, M. H.; Chong, W. K.; Liu, X.; Cai, Y.; Ding, H.; Asta, M.; Grätzel, M.; Mhaisalkar, S.; Mathews, N.; Sum, T. C.

- Solution-Processed Tin-Based Perovskite for Near-Infrared Lasing. *Adv. Mater.* **2016**, 28, 8191–8196.
- (12) Zhu, H.; Fu, Y.; Meng, F.; Wu, X.; Gong, Z.; Ding, Q.; Gustafsson, M. V.; Trinh, M. T.; Jin, S.; Zhu, X. Lead Halide Perovskite Nanowire Lasers with Low Lasing Thresholds and High Quality Factors. *Nat. Mater.* **2015**, *14*, 636–642.
- (13) Castañeda, J. A.; Nagamine, G.; Yassitepe, E.; Bonato, L. G.; Voznyy, O.; Hoogland, S.; Nogueira, A. F.; Sargent, E. H.; Brito Cruz, C. H.; Padilha, L. A. Efficient Biexciton Interaction in Perovskite Quantum Dots Under Weak and Strong Confinement. *ACS Nano* **2016**, 8603–8609.
- (14) Chen, J.; Liu, D.; Al-Marri, M. J.; Nuuttila, L.; Lehtivuori, H.; Zheng, K. Photo-Stability of CsPbBr3 Perovskite Quantum Dots for Optoelectronic Application. *Sci. China Mater.* **2016**, 719–727.
- (15) Dursun, I.; Shen, C.; Parida, M. R.; Pan, J.; Sarmah, S. P.; Priante, D.; Alyami, N.; Liu, J.; Saidaminov, M. I.; Alias, M. S.; et al. Perovskite Nanocrystals as a Color Converter for Visible Light Communication. *ACS Photonics* **2016**, *3*, 1150–1156.
- (16) Ravi, V. K.; Markad, G. B.; Nag, A. Band Edge Energies and Excitonic Transition Probabilities of Colloidal CsPbX<sub>3</sub> (X = Cl, Br, I) Perovskite Nanocrystals. *ACS Energy Lett.* **2016**, *1*, 665–671.
- (17) Yettapu, G. R.; Talukdar, D.; Sarkar, S.; Swarnkar, A.; Nag, A.; Ghosh, P.; Mandal, P. Terahertz Conductivity within Colloidal CsPbBr<sub>3</sub> Perovskite Nanocrystals: Remarkably High Carrier Mobilities and Large Diffusion Lengths. *Nano Lett.* **2016**, *16*, 4838–4848.
- (18) Luo, J.; Im, J.-H.; Mayer, M. T.; Schreier, M.; Nazeeruddin, M. K.; Park, N.-G.; Tilley, S. D.; Fan, H. J.; Grätzel, M. Water Photolysis at 12.3% Efficiency via Perovskite Photovoltaics and Earth-Abundant Catalysts. *Science* **2014**, *345*, 1593–1596.
- (19) Gurudayal; Sabba, D.; Kumar, M. H.; Wong, L. H.; Barber, J.; Grätzel, M.; Mathews, N. Perovskite—Hematite Tandem Cells for Efficient Overall Solar Driven Water Splitting. *Nano Lett.* **2015**, *15*, 3833—3839.
- (20) Bin, A. R.; Yusoff, M.; Jang, J. Highly Efficient Photoelectrochemical Water Splitting by A Hybrid Tandem Perovskite Solar Cell. *Chem. Commun.* **2016**, *52*, 5824–5827.
- (21) Dou, L.; Yang, Y. M.; You, J.; Hong, Z.; Chang, W.-H.; Li, G.; Yang, Y. Solution-Processed Hybrid Perovskite Photodetectors with High Detectivity. *Nat. Commun.* **2014**, *5*, No. 5404.
- (22) Hu, X.; Zhang, X.; Liang, L.; Bao, J.; Li, S.; Yang, W.; Xie, Y. High-Performance Flexible Broadband Photodetector Based on Organolead Halide Perovskite. *Adv. Funct. Mater.* **2014**, 24, 7373–7380
- (23) Fang, Y.; Dong, Q.; Shao, Y.; Yuan, Y.; Huang, J. Highly Narrowband Perovskite Single-Crystal Photodetectors Enabled by Surface-Charge Recombination. *Nat. Photonics* **2015**, *9*, 679–686.
- (24) Lee, Y., Kwon, J.; Hwang, E.; Ra, C. H.; Yoo, W. J.; Ahn, J. H.; Park, J. H.; Cho, J. H. High-Performance Perovskite—Graphene Hybrid Photodetector. *Adv. Mater.* **2015**, *27*, 41–46.
- (25) Zhuo, S.; Zhang, J.; Shi, Y.; Huang, Y.; Zhang, B. Self-Template-Directed Synthesis of Porous Perovskite Nanowires at Room Temperature for High-Performance Visible-Light Photodetectors. *Angew. Chem.* **2015**, *127*, 5785–5788.
- (26) Li, W.; Dong, H.; Dong, G.; Wang, L. Hystersis Mechanism in Perovskite Photovoltaic Devices and Its Potential Application for Multi-Bit Memory Devices. *Org. Electron.* **2015**, *26*, 208–212.
- (27) Yoo, E. J.; Lyu, M.; Yun, J. H.; Kang, C. J.; Choi, Y. J.; Wang, L. Resistive Switching Behavior in Organic–Inorganic Hybrid CH<sub>3</sub>NH<sub>3</sub>PbI<sub>3-x</sub>Cl<sub>x</sub> Perovskite for Resistive Random Access Memory Devices. *Adv. Mater.* **2015**, 27, 6170–6175.
- (28) Wawro, A.; Sobańska, M.; Petroutchik, A.; Baczewski, L.; Pankowski, P. Self-Assembled Growth of Au Islands on a Mo (110) Surface. *Nanotechnology* **2010**, *21*, No. 335606.
- (29) Wang, X.-D.; Li, W.-G.; Liao, J.-F.; Kuang, D.-B. Recent Advances in Halide Perovskite Single-Crystal Thin Films: Fabrication Methods and Optoelectronic Applications. *Solar RRL* **2019**, No. 1800294.
- $(30) \ https://www.nrel.gov/pv/assets/pdfs/best-reserch-cell-efficiencies.pdf.$

- (31) Rahimnejad, S.; Kovalenko, A.; Forés, S. M.; Aranda, C.; Guerrero, A. Coordination chemistry dictates the structural defects in lead halide perovskites. *ChemPhysChem* **2016**, *17*, 2795–2798.
- (32) Ball, J. M.; Petrozza, A. Defects in perovskite-halides and their effects in solar cells. *Nat. Energy* **2016**, *1*, No. 16149.
- (33) Wu, X.; Trinh, M. T.; Niesner, D.; Zhu, H.; Norman, Z.; Owen, J. S.; Yaffe, O.; Kudisch, B. J.; Zhu, X.-Y. Trap states in lead iodide perovskites. J. Am. Chem. Soc. 2015, 137, 2089–2096.
- (34) Benmessaoud, I. R.; Mahul-Mellier, A.-L.; Horvath, E.; Maco, B.; Spina, M.; Lashuel, H. A.; Forro, L. Health Hazards of Methylammonium Lead Iodide Based Perovskites: Cytotoxicity Studies. *Toxicol. Res.* **2016**, *5*, 407–419.
- (35) Grätzel, M. The Light and Shade of Perovskite Solar Cells. *Nat. Mater.* **2014**, *13*, 838–842.
- (36) Christians, J. A.; Miranda Herrera, P. A.; Kamat, P. V. Transformation of the Excited State and Photovoltaic Efficiency of CH<sub>3</sub>NH<sub>3</sub>PbI<sub>3</sub> Perovskite Upon Controlled Exposure to Humidified Air. J. Am. Chem. Soc. **2015**, 137, 1530–1538.
- (37) Conings, B.; Drijkoningen, J.; Gauquelin, N.; Babayigit, A.; D'Haen, J.; D'Olieslaeger, L.; Ethirajan, A.; Verbeeck, J.; Manca, J.; Mosconi, E.; et al. Intrinsic Thermal Instability of Methylammonium Lead Trihalide Perovskite. *Adv. Energy Mater.* **2015**, *5*, No. 1500477.
- (38) Misra, R. K.; Aharon, S.; Li, B.; Mogilyansky, D.; Visoly-Fisher, I.; Etgar, L.; Katz, E. A. Temperature-and Component-Dependent Degradation of Perovskite Photovoltaic Materials Under Concentrated Sunlight. J. Phys. Chem. Lett. 2015, 6, 326–330.
- (39) Yang, J.; Siempelkamp, B. D.; Liu, D.; Kelly, T. L. Investigation of CH<sub>3</sub>NH<sub>3</sub>PbI<sub>3</sub> Degradation Rates and Mechanisms in Controlled Humidity Environments Using In Situ Techniques. *ACS Nano* **2015**, 9, 1955–1963.
- (40) Jellicoe, T. C.; Richter, J. M.; Glass, H. F.; Tabachnyk, M.; Brady, R.; Dutton, S. E.; Rao, A.; Friend, R. H.; Credgington, D.; Greenham, N. C.; Böhm, M. L. Synthesis and optical properties of lead-free cesium tin halide perovskite nanocrystals. *J. Am. Chem. Soc.* **2016**, *138*, 2941–2944.
- (41) Moghe, D.; Wang, L.; Traverse, C. J.; Redoute, A.; Sponseller, M.; Brown, P. R.; Bulović, V.; Lunt, R. R. All vapor-deposited lead-free doped CsSnBr<sub>3</sub> planar solar cells. *Nano Energy* **2016**, *28*, 469–474.
- (42) Gupta, S.; Bendikov, T.; Hodes, G.; Cahen, D. CsSnBr<sub>3</sub>, A Lead-Free Halide Perovskite for Long-Term Solar Cell Application: Insights on SnF<sub>2</sub> Addition. ACS Energy Lett. **2016**, 1, 1028–1033.
- (43) Chen, Z.; Wang, J. J.; Ren, Y.; Yu, C.; Shum, K. Schottky solar cells based on CsSnI3 thin-films. *Appl. Phys. Lett.* **2012**, *101*, No. 093901.
- (44) Marshall, K. P.; Walker, M.; Walton, R. I.; Hatton, R. A. Enhanced stability and efficiency in hole-transport-layer-free CsSnI<sub>3</sub> perovskite photovoltaics. *Nat. Energy* **2016**, *1*, No. 16178.
- (45) The Cambridge Structural Database (CSD).
- (46) Chung, I.; Song, J.-H.; Im, J.; Androulakis, J.; Malliakas, C. D.; Li, H.; Freeman, A. J.; Kenney, J. T.; Kanatzidis, M. G. CsSnI3: Semiconductor or Metal? High Electrical Conductivity and Strong Near-Infrared Photoluminescence from a Single Material. High Hole Mobility and Phase-Transitions. *J. Am. Chem. Soc.* **2012**, *134*, 8579–8587.
- (47) Kumar, M. H.; Dharani, S.; Leong, W. L.; Boix, P. P.; Prabhakar, R. R.; Baikie, T.; Shi, C.; Ding, H.; Ramesh, R.; Asta, M.; et al. Lead-Free Halide Perovskite Solar Cells with High Photocurrents Realized Through Vacancy Modulation. *Adv. Mater.* **2014**, 7122.
- (48) Hwang, H. Y.; Iwasa, Y.; Kawasaki, M.; Keimer, B.; Nagaosa, N.; Tokura, Y. Emergent phenomena at oxide interfaces. *Nat. Mater.* **2012**, *11*, 103.
- (49) Schlom, D. G.; Chen, L.-Q.; Fennie, C. J.; Gopalan, V.; Muller, D. A.; Pan, X.; Ramesh, R.; Uecker, R. Elastic strain engineering of ferroic oxides. *MRS Bull.* **2014**, *39*, 118–130.
- (50) Carpenter, M. In Strain Coupling and Dynamic Relaxation Dynamics Associated with Ferroic and Multiferroic Phase Transition, APS Meeting Abstracts, 2016.

- (51) Mundy, J. A.; Brooks, C. M.; Holtz, M. E.; Moyer, J. A.; Das, H.; Rébola, A. F.; Heron, J. T.; Clarkson, J. D.; Disseler, S. M.; Liu, Z.; et al. Atomically engineered ferroic layers yield a room-temperature magnetoelectric multiferroic. *Nature* **2016**, *537*, *523*.
- (52) Si, W.; Jie, Q.; Wu, L.; Zhou, J.; Gu, G.; Johnson, P. D.; Li, Q. Superconductivity in epitaxial thin films of Fe<sub>1.08</sub>Te:O<sub>x</sub>. *Phys. Rev. B* **2010**, *81*, No. 092506.
- (53) Ou, Y.; Nandi, D.; Huang, K.; Ozsoy-Keskinbora, C.; Kraemer, S.; Bell, D.; Kim, P.; Yacoby, A.; Moodera, J. In Molecular Beam Epitaxy Growth and Properties of Strained Superconducting Half-Heusler LaPtBi Film, a Candidate Topological Superconductor, APS Meeting Abstracts, 2018.
- (54) Asaba, T.; Wang, Y.; Li, G.; Xiang, Z.; Tinsman, C.; Chen, L.; Zhou, S.; Zhao, S.; Laleyan, D.; Li, Y.; et al. Magnetic Field Enhanced Superconductivity in Epitaxial Thin Film WTe<sub>2</sub>. Sci. Rep. **2018**, 8, No. 6520.
- (55) Wang, J.; Neaton, J. B.; Zheng, H.; Nagarajan, V.; Ogale, S. B.; Liu, B.; Viehland, D.; Vaithyanathan, V.; Schlom, D. G.; Waghmare, U. V.; et al. Epitaxial BiFeO<sub>3</sub> multiferroic thin film heterostructures. *Science* **2003**, 299, 1719–1722.
- (56) Béa, H.; Bibes, M.; Ott, F.; Dupé, B.; Zhu, X.-H.; Petit, S.; Fusil, S.; Deranlot, C.; Bouzehouane, K.; Barthélémy, A. Mechanisms of exchange bias with multiferroic BiFeO 3 epitaxial thin films. *Phys. Rev. Lett.* **2008**, *100*, No. 017204.
- (57) Wang, L.; Chen, P.; Thongprong, N.; Young, M.; Kuttipillai, P. S.; Jiang, C.; Zhang, P.; Sun, K.; Duxbury, P. M.; Lunt, R. R. Unlocking the Single-Domain Epitaxy of Halide Perovskites. *Adv. Mater. Interfaces* **2017**, *4*, No. 1701003.
- (58) Wang, Y.; Sun, X.; Chen, Z.; Sun, Y. Y.; Zhang, S.; Lu, T. M.; Wertz, E.; Shi, J. High-Temperature Ionic Epitaxy of Halide Perovskite Thin Film and the Hidden Carrier Dynamics. *Adv. Mater.* **2017**, 29, No. 1702643.
- (59) Chen, J.; Morrow, D. J.; Fu, Y.; Zheng, W.; Zhao, Y.; Dang, L.; Stolt, M. J.; Kohler, D. D.; Wang, X.; Czech, K. J.; et al. Single-crystal thin films of cesium lead bromide perovskite epitaxially grown on metal oxide perovskite (SrTiO<sub>3</sub>). *J. Am. Chem. Soc.* **2017**, *139*, 13525–13532.
- (60) Li, X.; Luo, Y.; Holt, M. V.; Cai, Z.; Fenning, D. P. Residual Nanoscale Strain in Cesium Lead Bromide Perovskite Reduces Stability and Shifts Local Luminescence. *Chem. Mater.* **2019**, 2778–2785.
- (61) Srinivasan, R. Thermal Expansion of Sodium and Potassium Chlorides from Liquid-air Temperatures to +300° C. *J. Indian Inst. Sci.* **2013**, *37*, 232.
- (62) Wang, A.; Yan, X.; Zhang, M.; Sun, S.; Yang, M.; Shen, W.; Pan, X.; Wang, P.; Deng, Z. Controlled Synthesis of Lead-Free and Stable Perovskite Derivative Cs<sub>2</sub>SnI<sub>6</sub> Nanocrystals via a Facile Hot-Injection Process. *Chem. Mater.* **2016**, 28, 8132–8140.
- (63) Zhang, J.; Yu, C.; Wang, L.; Li, Y.; Ren, Y.; Shum, K. Energy barrier at the N719-dye/CsSnI<sub>3</sub> interface for photogenerated holes in dye-sensitized solar cells. *Sci. Rep.* **2015**, *4*, No. 6954.
- (64) Da Silva, E. L.; Skelton, J. M.; Parker, S. C.; Walsh, A. Phase stability and transformations in the halide perovskite CsSnI<sub>3</sub>. *Phys. Rev. B* **2015**, *91*, No. 144107.
- (65) Chopra, K. L. Metastable Thin Film Epitaxial Structures. *Phys. Status Solidi B* **1969**, 32, 489–507.
- (66) Peedikakkandy, L.; Bhargava, P. Composition dependent optical, structural and photoluminescence characteristics of cesium tin halide perovskites. *RSC Adv.* **2016**, *6*, 19857–19860.
- (67) Chen, P.; Kuttipillai, P. S.; Wang, L.; Lunt, R. R. Homoepitaxial Growth of Metal Halide Crystals Investigated by Reflection High-Energy Electron Diffraction. *Sci. Rep.* **2017**, *7*, No. 40542.
- (68) Liu, D.; Wang, Q.; Elinski, M.; Chen, P.; Traverse, C. J.; Yang, C.; Young, M.; Hamann, T. W.; Lunt, R. R. Ultrathin Hole Extraction Layer for Efficient Inverted Perovskite Solar Cells. *ACS Omega* **2018**, 3, 6339–6345.
- (69) Wang, Y.; Song, Q.; Lin, T.; Fu, Y.; Sun, X.; Chu, B.; Jin, F.; Zhao, H.; Li, W.; Su, Z.; Li, Y. Improved performance of

CH<sub>3</sub>NH<sub>3</sub>PbI<sub>3</sub> based photodetector with a MoO<sub>3</sub> interface layer. *Org. Electron.* **2017**, *49*, 355–359. (70) Ji, C.; Kim, K.; Oh, S. High-detectivity perovskite-based photodetector using a Zr-doped  ${\rm TiO_x}$  cathode interlayer. *RSC Adv.* **2018**, *8*, 8302–8309.

# SUPPLEMENTARY INFORMATION

# Epitaxial Stabilization of Tetragonal Cesium Tin

# Iodide

Lili Wang†, Pei Chen†, Padmanaban S. Kuttipillai†, Isaac King†, Richard Staples‡, Kai Sun<sup>||</sup>, and Richard R. Lunt\* †, §

†Department of Chemical Engineering and Materials Science, Michigan State University

East Lansing, MI 48824 USA

<sup>‡</sup>Department of Chemistry, Michigan State University

East Lansing, MI 48824 USA

 $^{/\!\!/}$  Department of Materials Science and Engineering, University of Michigan

Ann Arbor, MI 48109 USA

§Department of Physics and Astronomy, Michigan State University

East Lansing, MI 48824 USA

**Table S1.** Crystal structures, lattice parameters, experimental and simulated bandgaps of the cubic, tetragonal, orthorhombic and the epi-tetragonal phase from this work. Band structure and

<sup>\*</sup>rlunt@msu.edu

bandgap calculations were performing using the CASTEP module in Material Studio 7.0 with the B3LYP functional.

Phase	Cubic (High <i>T</i> )	Tetragonal (High <i>T</i> )	Orthorhombic (Room <i>T</i> )	Epi-tetragonal (Room <i>T</i> , this work)
Crystal Structure  Cs Sn I				
Lattice Parameters(nm)	a=0.62057	<i>a</i> = <i>b</i> =0.87182, <i>c</i> =0.61908	a=0.86885, b=1.23775, c=0.86384	a=b=0.622±0.007, c=0.612±0.002
Experimental Bandgap (eV)	-	-	1.31 <sup>2</sup>	1.85
Simulated Bandgap (eV)	0.76	0.41	1.40	2.07

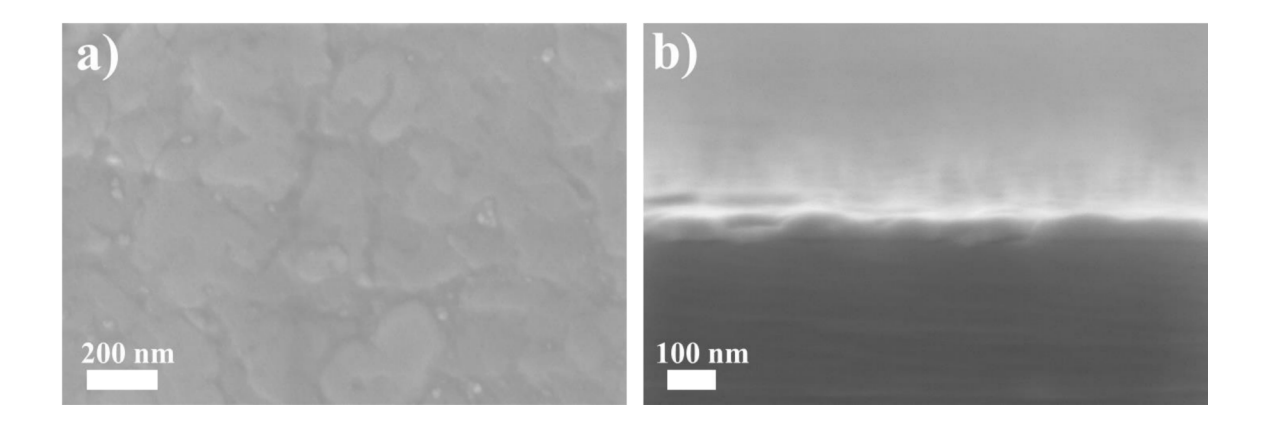


**Figure S1.** (A) Scanning electron microscope (SEM) and (B) cross-section SEM image of 40nm epitaxial CsSnI<sub>3</sub> on KCl.

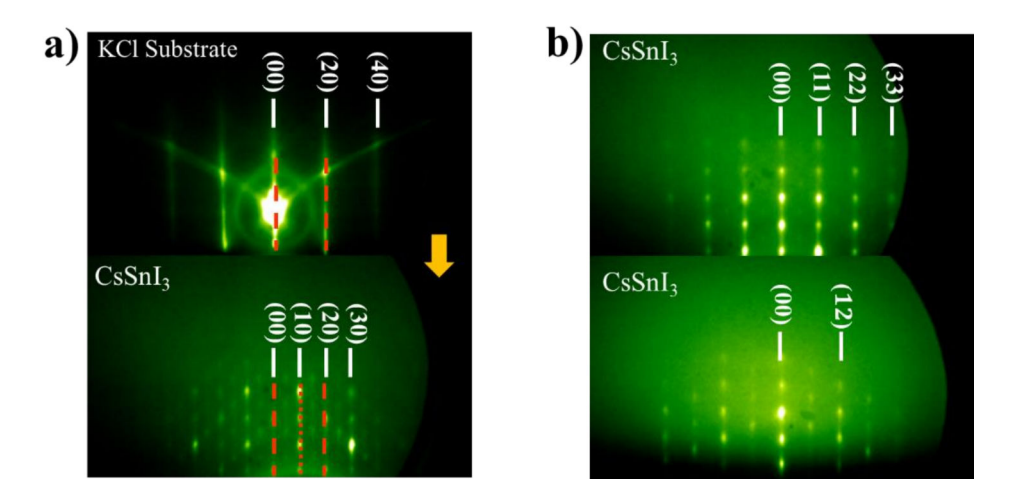


**Figure S2.** (A) Reflection high-energy electron diffraction (RHEED) pattern of the bare KCl substrate and 20nm of CsSnI<sub>3</sub> grown at high rate. The spotty pattern indicates the film is crystalline and rough. (B) Rotation dependent RHEED patterns of the rough CsSnI<sub>3</sub> epitaxial film.

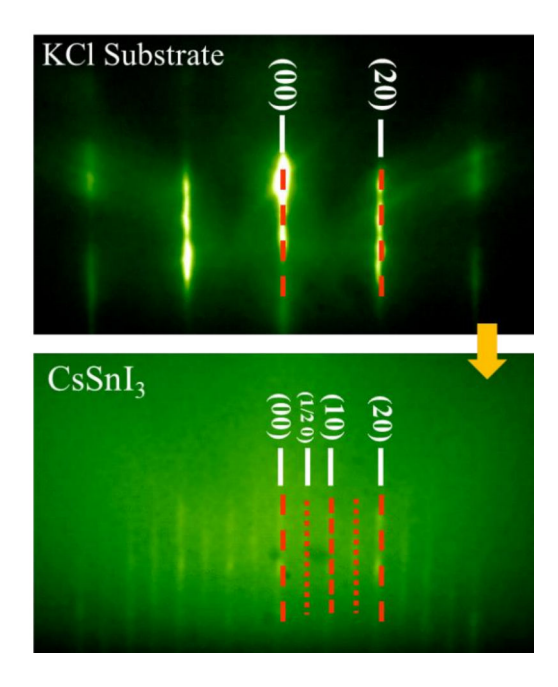


**Figure S3.** RHEED pattern of the bare KCl substrate and 20nm of CsSnI<sub>3</sub>. Half-order streaks are occasionally observed at high growth rate indicating a surface reconstruction of the perovskite monolayer.

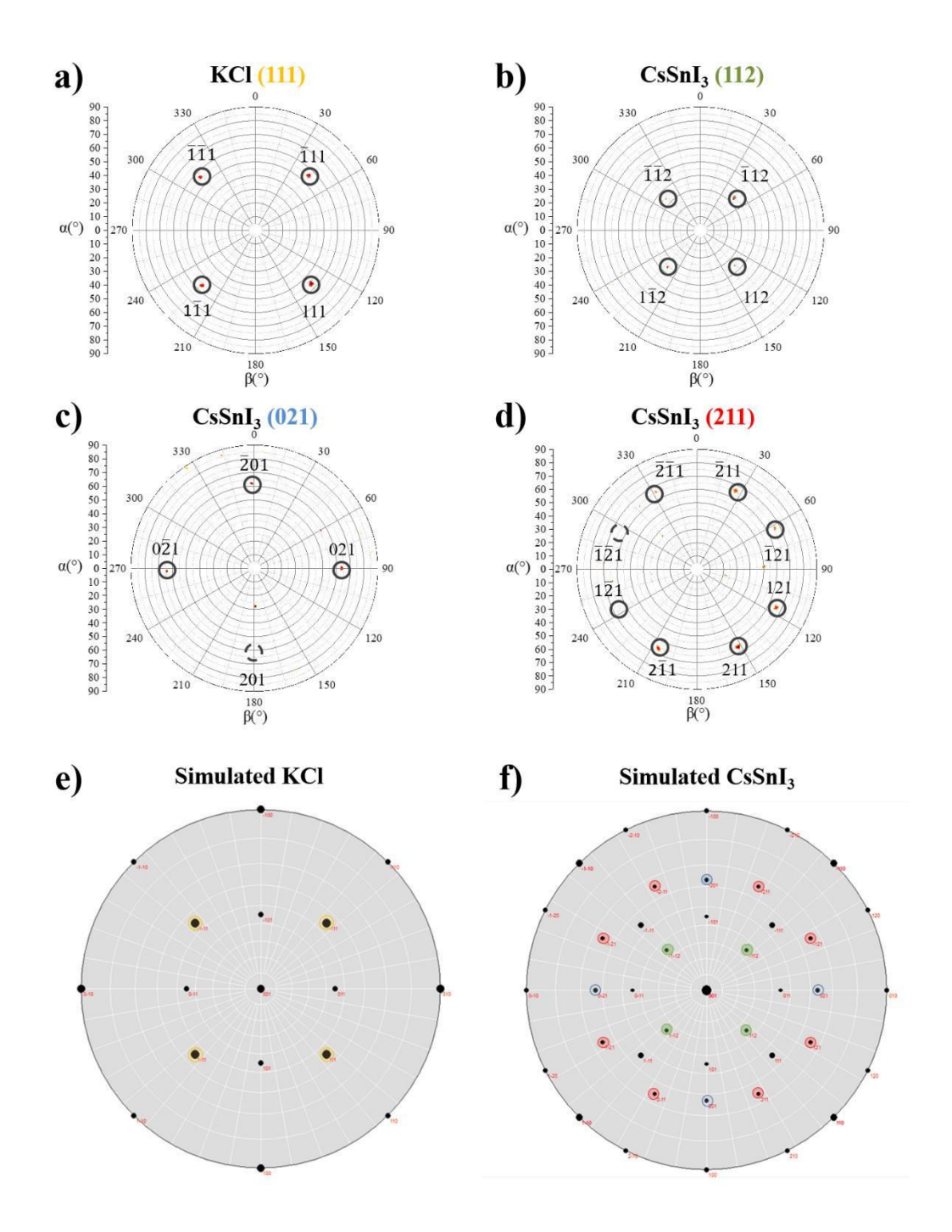


**Figure S4.** (A) The (111) pole figure scan of KCl substrate. (B-D) The (112) (021) (112) pole figure scan of 40nm of CsSnI<sub>3</sub> on KCl substrate.  $\alpha$  and  $\beta$  are tilt and rotation angles around the sample surface normal direction. (E-F) Simulated pole figure of KCl and epi-tetragonal CsSnI<sub>3</sub>, which are in good agreement with the experimental scans. Note that a couple of the (211) are missing due to slight tilt of the crystal. The (112) (021) (112) poles for epi-tetragonal CsSnI<sub>3</sub> are clearly distinguishable from the KCl substrate.

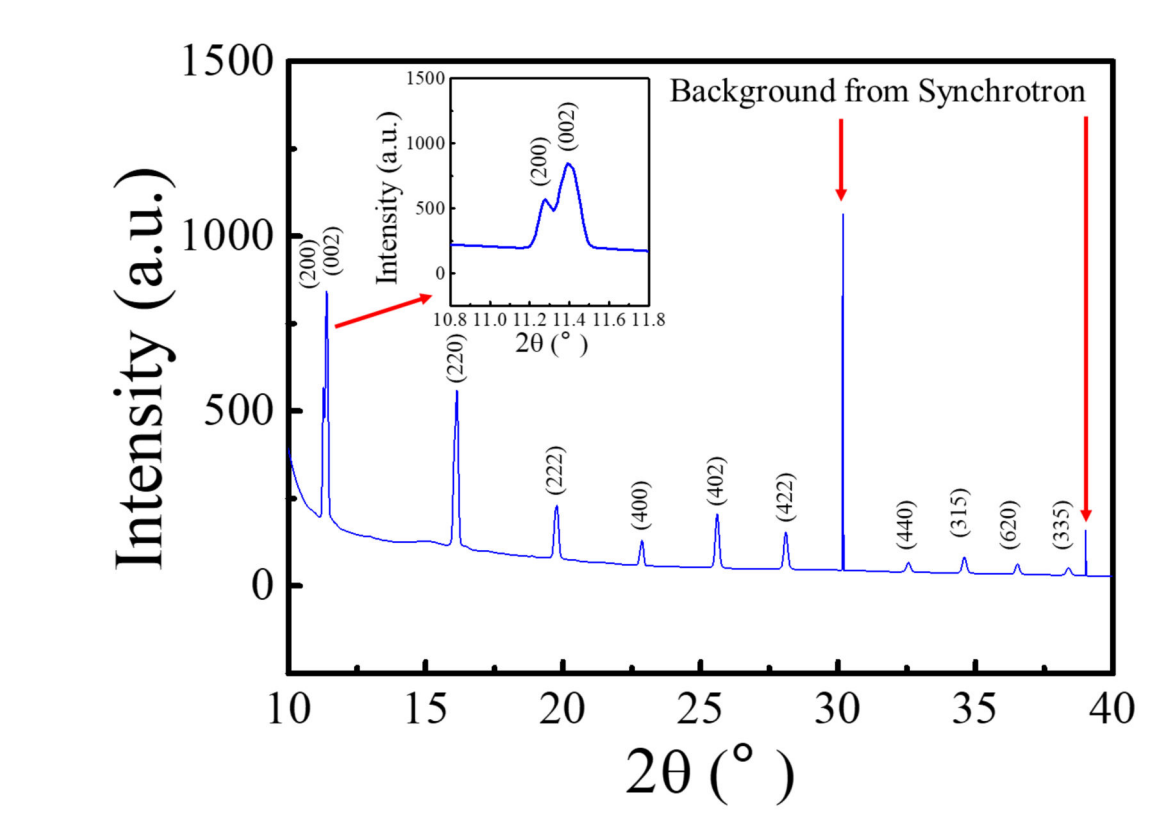


**Figure S5.** Synchrotron X-ray diffraction (XRD) patterns of 20nm of CsSnI<sub>3</sub> removed from the substrate and formed into a folded (textured pseudo-powder) film. An obvious peak split is seen at 11.28° and 11.39° (inset), which corresponds to the (200) and (002) planes of the epi-tetragonal phase respectively.

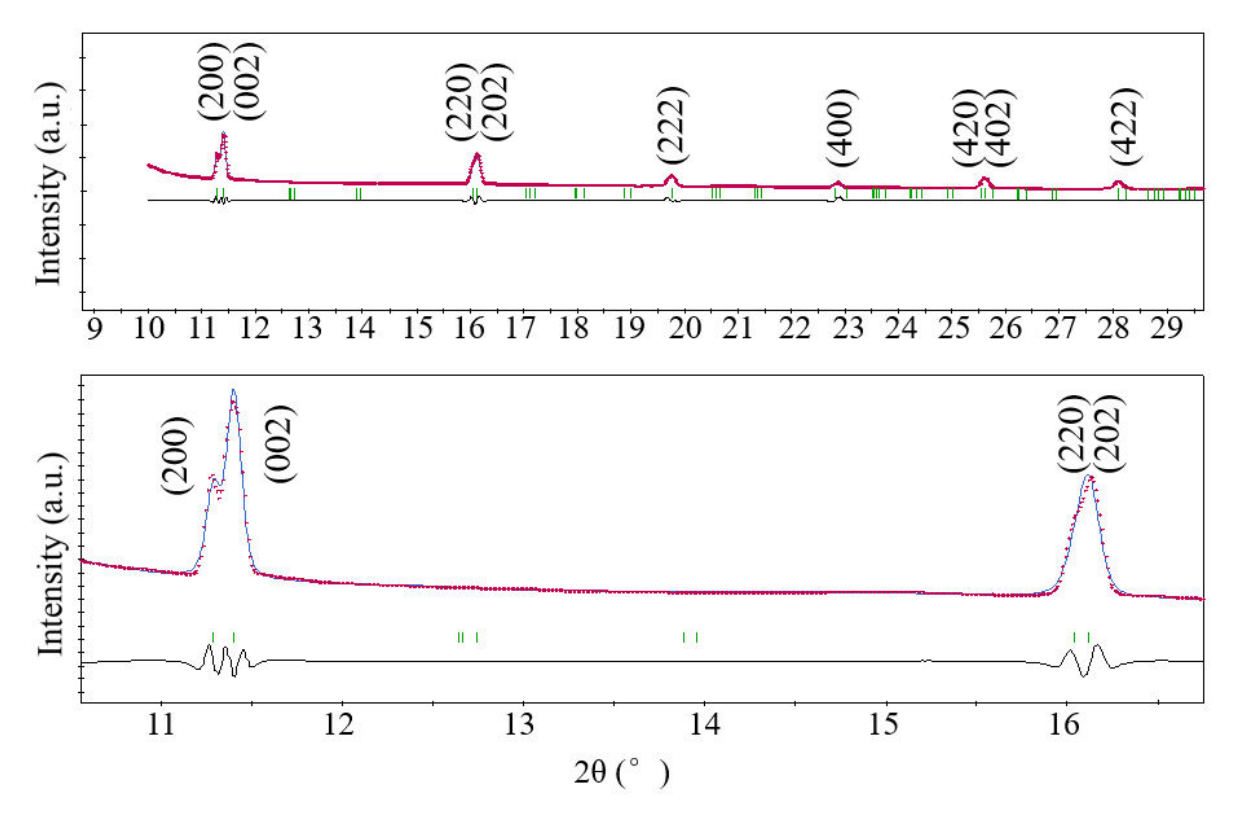


**Figure S6.** (top) The refinement and fitting of the synchrotron ( $\lambda = 0.0619870$ nm) XRD pattern using the Pawley method in Materials Studio. Lattice constants of the epitaxial CsSnI<sub>3</sub> film obtained from the fitting are a = b = 0.6240nm, c = 0.6178nm. Note the blue line is the fit, red dots are the data, and the black line is the difference between the experimental data and the fit. (bottom) Zoom-in of the plot on top highlighted the region around the (200)/(002) and (220)/(202) peaks.

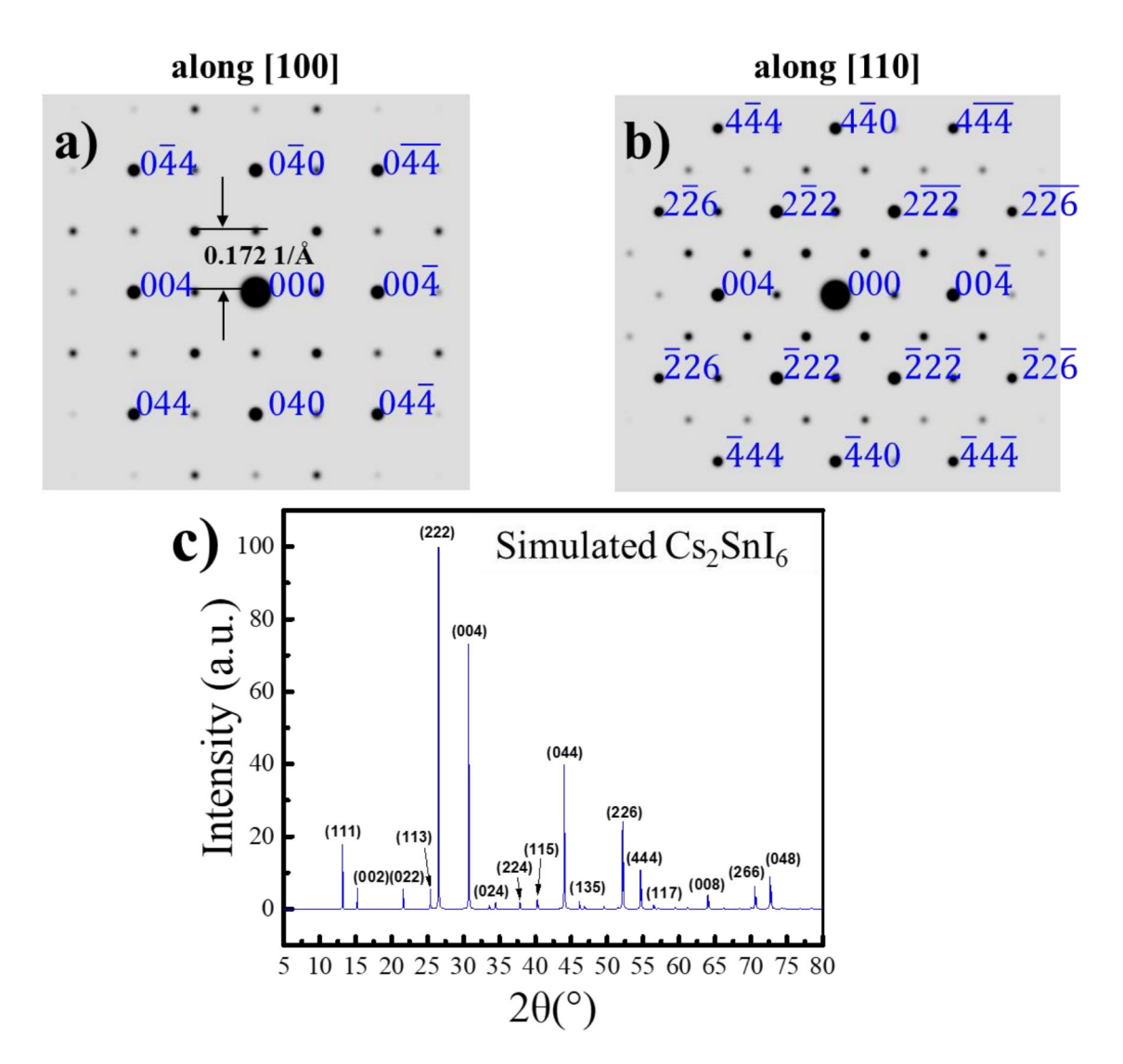


**Figure S7.** (A-B) Simulated selected area electron diffraction (SAED) patterns of Cs<sub>2</sub>SnI<sub>6</sub>. (C) Simulated XRD pattern of Cs<sub>2</sub>SnI<sub>6</sub>.

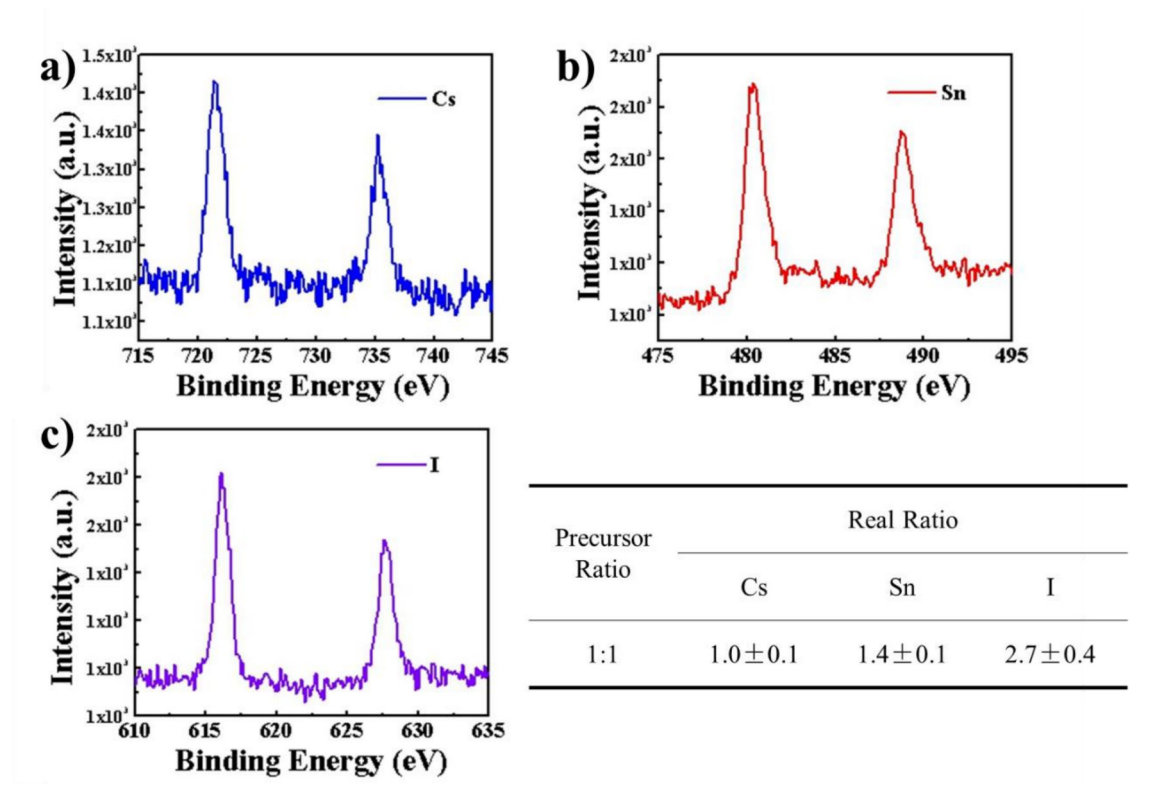


**Figure S8.** X-ray Photoelectron Spectroscopy (XPS) spectra of (A) Cs (B) Sn and (C) I for the epitaxial CsSnI<sub>3</sub> film. The ratio matches with the stoichiometry of CsSnI<sub>3</sub> and the Sn is found to have a +2 valence state in the epitaxial film.

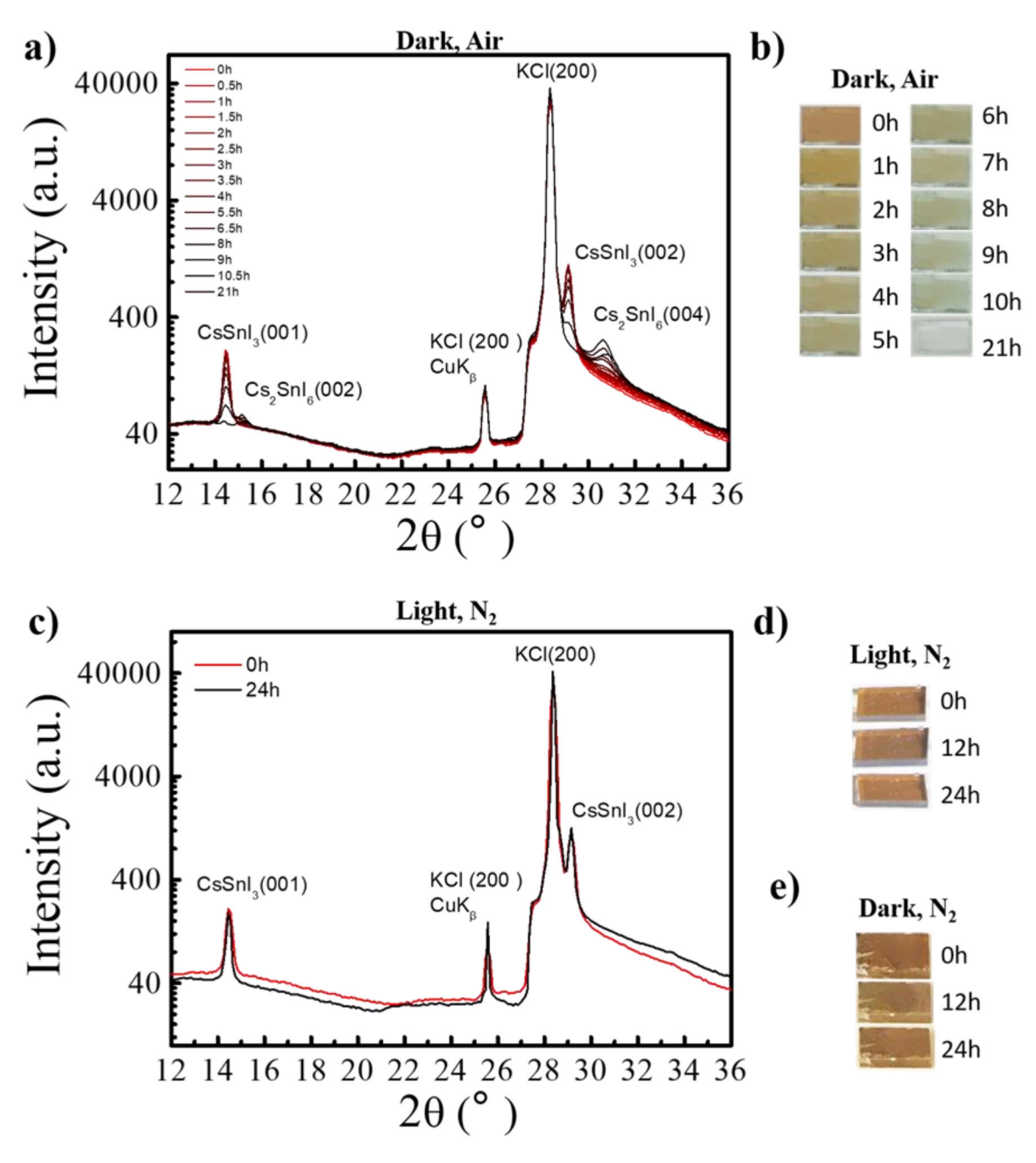


**Figure S9.** (A) XRD patterns and (B) color change of an epitaxial  $CsSnI_3$  film (40nm) on KCl as a function of time in the dark and exposed to air. (C) XRD patterns and (D) color change of an epitaxial  $CsSnI_3$  film (40nm) on KCl as a function of time under light soaking and in  $N_2$ . (E) Color change of an epitaxial  $CsSnI_3$  film (40nm) on KCl as a function of time in dark and in  $N_2$ .

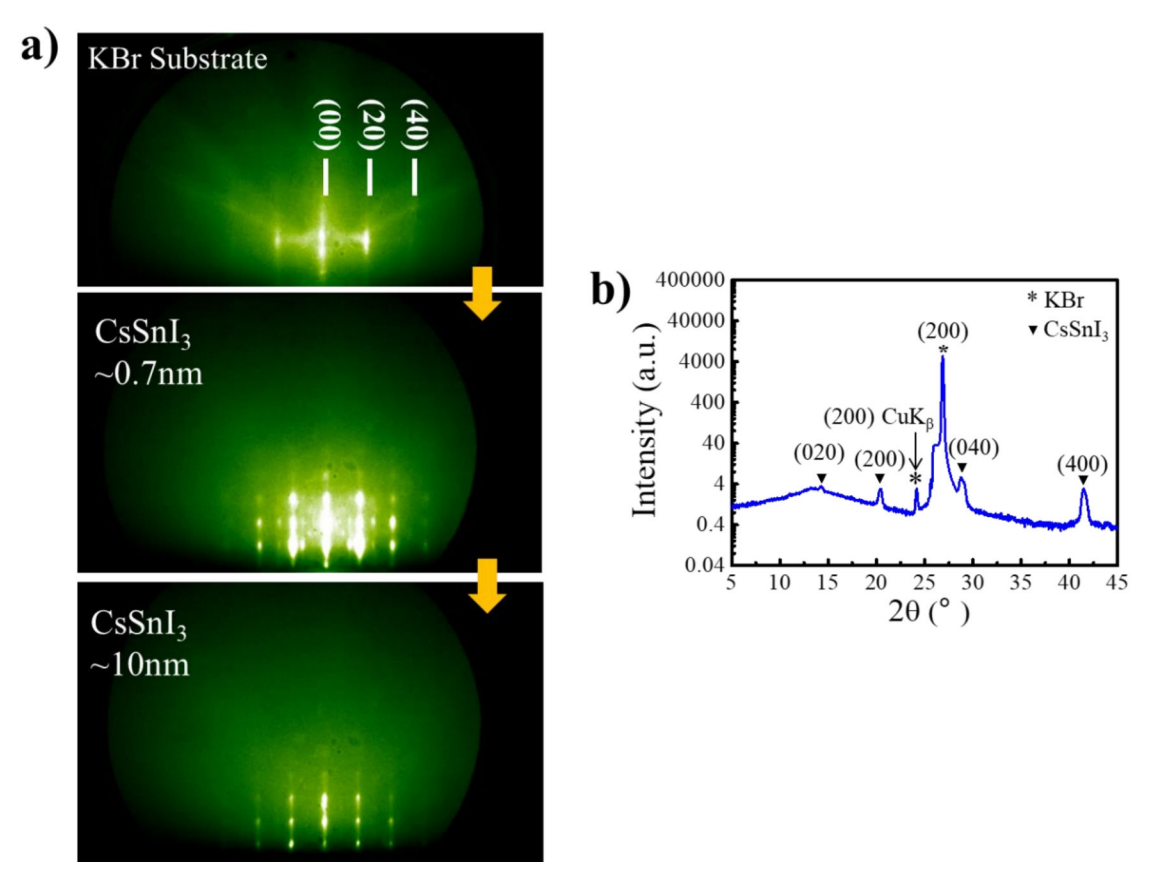


**Figure S10.** (A) RHEED pattern of the bare KBr substrate and CsSnI<sub>3</sub> at low and high thickness. Multiple rotational domains are seen during the initial growth. (B) Out-of-plane XRD scan of 40nm of CsSnI<sub>3</sub> on KBr. Both the XRD and RHEED data are consistent with the typical room-temperature orthorhombic phase.

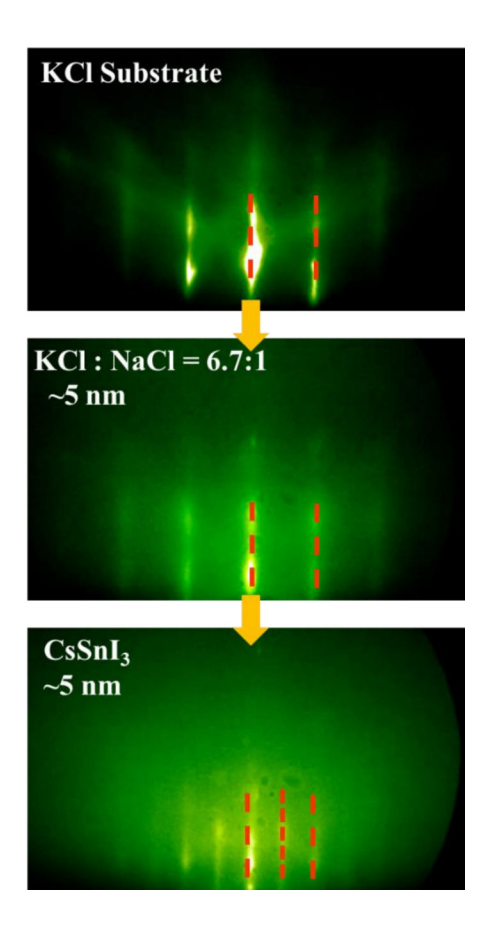


**Figure S11.** RHEED pattern of the bare KCl substrate, the alloyed growth of 5 nm of KCl and NaCl (6.7:1) and 5 nm of  $CsSnI_3$ .

# **REFERENCES**

- (1) The Cambridge Structural Database (CSD).
- (2) Peedikakkandy, L.; Bhargava, P. Composition dependent optical, structural and photoluminescence characteristics of cesium tin halide perovskites. *RSC Adv.* **2016**, *6* (24), 19857-19860.